Supporting Information

From Monolayer to Thin Film Engineered Bandgap in CVD Grown Bi$_2$Se$_{(3-x)}$S$_x$ Topological Insulator Alloys

Michal Poplinger[1,2], Dimitris Kaltsas[3], Chen Stern[1,2], Pilkhaz Nanikashvili[1,2], Adi Levi[1,2], Rajesh K. Yadav[1,2], Sukanta Nandi[1,2], Yuxiao Wu[2,4], Avinash Patsha[5], Ariel Ismach[5], Ashwin Ramasubramaniam[6,7], Amaia Pesquera[8], Amaia Zurutuza[8], Ioanna Zergioti[3], Leonidas Tsetseris[3], Tomer Lewi[1,2] and Doron Naveh[1,2]*

[1] Faculty of Engineering, Bar-Ilan University, Israel

[2] Institute for Nanotechnology and Advanced Materials, Bar-Ilan University, Israel

[3] Department of Physics, School of Applied Mathematical and Physical Sciences, National Technical University of Athens, Athens, Greece

[4] Department of Physics, Faculty of Exact Sciences, Bar-Ilan University, Israel

[5] Department of Materials Science and Engineering, Tel Aviv University, Ramat Aviv, Tel Aviv 6997801, Israel

[6] Department of Mechanical and Industrial Engineering, University of Massachusetts Amherst, U.S.A

[7] Materials Science and Engineering Graduate Program, University of Massachusetts Amherst, U.S.A

[8] Graphenea Headquarters, Spain

[*]Corresponding author: doron.naveh@biu.ac.il

1. **Bi$_2$Se$_{(3-x)}$S$_x$ synthesis**

1.1. Samples pre-cleaning

Before the CVD growth process, the substrates that were not covered with graphene, i.e., sapphire and Si/SiO$_2$, were pre-treated in an ultrasonic bath with acetone and isopropyl alcohol for 5 minutes to remove contaminants. To remove organic residues from the surface, the substrates were treated in a sulfuric peroxide solution (H$_2$SO$_4$:H$_2$O$_2$) in a ratio of 3:1 at 90°C for 15 minutes, followed by a wash in deionized water.
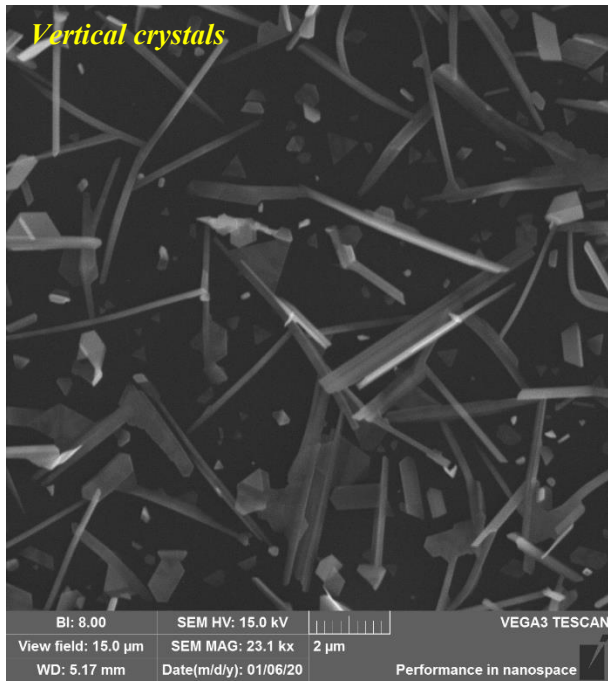
1.2. CVD process

Bi$_2$Se$_{(3-x)}$S$_x$ was synthesized by the CVD method in a tube furnace, inside a quartz tube. The starting precursors for the CVD synthesis were Bi$_2$Se$_3$ powder (Alfa Aesar – 99.999%) and sulfur powder (Sigma Aldrich – 99.5%). Bi$_2$Se$_3$ was placed in a quartz boat at the center of the furnace. The sulfur was placed 25 cm upstream of the Bi$_2$Se$_3$ source and was kept in the liquid phase during the growth. The substrates on which Bi$_2$Se$_{(3-x)}$S$_x$ was grown were located downstream at different distances from the precursor Bi$_2$Se$_3$. Their distance from the center of the furnace and the temperature of the Bi$_2$Se$_3$ precursor determined the temperature of the substrates (see **Table 1** of the main text).
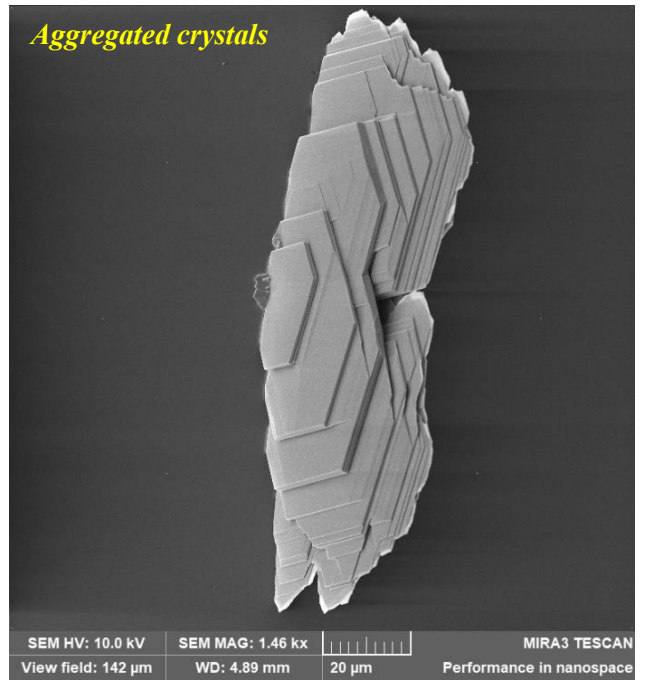
Before the growth, the quartz tube was evacuated to a vacuum pressure of 10 mTorr and was held at a temperature of 200°C for 60 minutes, under an N$_2$ flow of 100 sccm. Then, the oven temperature was set to the growth temperature (see **Table 1**) at 20°C/min, and the sulfur temperature was set to 140°C. The growth time (**Table 1**), under an N$_2$ flow of 5 sccm, ended with the gradual cooling of the chamber (5°C/min) and spontaneous cooling of the sulfur.
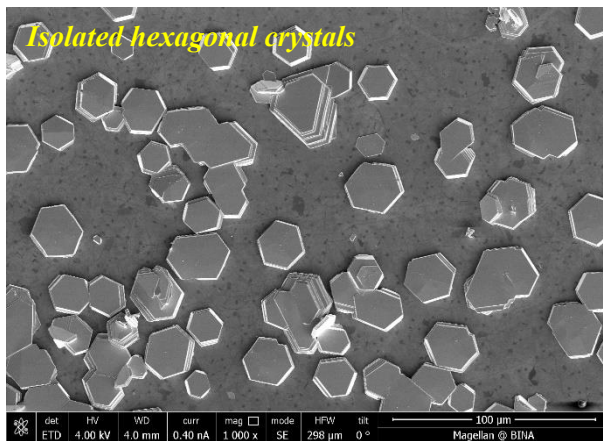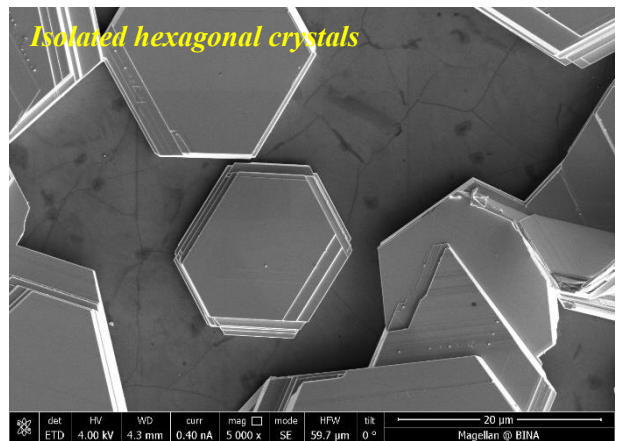
1.3. Bi$_2$Se$_{(3-x)}$S$_x$ morphology

(a)

Vertical crystals

BI: 8.00	SEM HV: 15.0 kV		VEGA3 TESCAN
View field: 15.0 µm	SEM MAG: 23.1 kx	2 µm	
WD: 5.17 mm	Date(m/d/y): 01/06/20		Performance in nanospace

(b)

Aggregated crystals

SEM HV: 10.0 kV	SEM MAG: 1.46 kx		MIRA3 TESCAN
View field: 142 µm	WD: 4.89 mm	20 µm	Performance in nanospace

(c)

Isolated hexagonal crystals

	det	HV	WD	curr	mag ☐	mode	HFW	tilt	100 µm
	ETD	4.00 kV	4.0 mm	0.40 nA	1 000 x	SE	298 µm	0 °	Magellan @ BINA

(d)

Isolated hexagonal crystals

	det	HV	WD	curr	mag ☐	mode	HFW	tilt	20 µm
	ETD	4.00 kV	4.3 mm	0.40 nA	5 000 x	SE	59.7 µm	0 °	Magellan @ BINA

**(e)**

Figure S1. $Bi_2Se_{(3-x)}S_x$ morphologies by SEM images on various substrates: (a) Si/SiO_2, (b) sapphire, and monolayer graphene on Si/SiO_2 grown for (c) 60 minutes, (d) 120 minutes, and (e) 180 minutes.

2. <u>Mass spectroscopy mapping of the grown $Bi_2Se_{(3-x)}S_x$ crystals</u>

Time-of-flight secondary ion mass spectroscopy (PHI 2100 TRIFT II) measurements were performed using a Ga^+ ion beam. Surface mass spectra and depth profiles were collected. The depth profiling was performed in a dual-beam mode. A 15KeV Ga^+ (current of 600pA) ion beam was used as an analytical beam, and a 500eV Cs^+ (current of 50nA) ion beam was used for sputtering. The analyzed area was 50 x 50 μm^2, and the sputtered area was 400 x 400 μm^2. The analysis was performed in the vacuum of 5 x 10^{-10} Torr and negative ions mode.
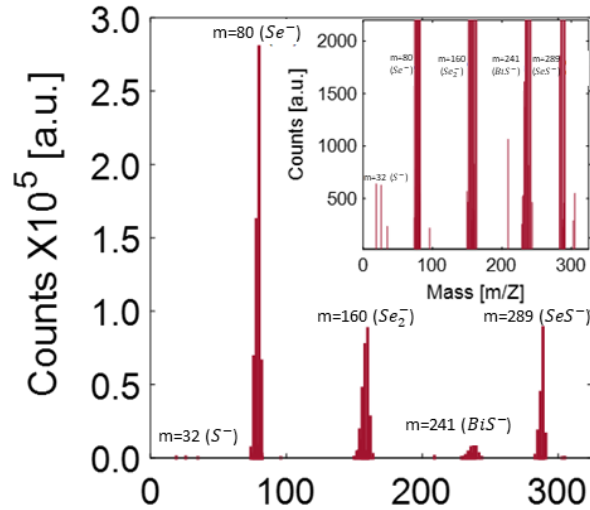
Figure S2. TOF-SIMS spectra showing the mass fractions of the main ions obtained. The inset shows the magnified low signal intensity region.

3. Diffusion processes of chalcogen atoms

Several possible (intralayer) diffusion processes that are relevant to the formation of $Bi_2Se_{(3-x)}S_x$ alloys were investigated in order to probe the kinetics of chalcogen atoms during growth. To simulate the so-called minimum energy pathway (MEP) for each process we used the nudged elastic band method[1] (NEB) with intermediate structures (also called images within NEB) between the initial and final configurations (the number of these intermediate structures corresponds to the numbers of filled circles shown in the NEB graphs of the following figures). The configuration with the highest energy in this "chain" of structures gives the transition state (TS) of the process. The difference between the energy of the TS and the energy of the initial (or final) configuration gives the barrier of the process (or, equivalently, the activation energy of the NEB images corresponds to an effective reaction (process) coordinate, whose value of 0 (1) relates to the initial (final) structure of the process). Because the NEB calculations are computationally demanding, they employed only the Gamma point for j-point sampling.

Figure S3a shows the migration of a vacancy from a position in the middle of a QL to a position on the outside (V^{Se2}-V^{Se1}). The calculated energy barrier is 1.99 eV and there is an energy difference of 0.24 eV between the initial and final positions with V^{Se2} being less stable (**Figure S3a**). Further calculations using 2 x 2 x 1 k-grids for the V^{Se2} and V^{Se1} configurations gave an energy difference of 0.39 eV in agreement with previous DFT studies that found 0.40 eV.[2–6] This high energy barrier for a vacancy to migrate between the middle and outer layers suggests that

5

vacancies that are formed in Se2 positions during the early stages of crystal growth, may become trapped in the middle of the QL despite the fact that V^{Se1} is more stable. A previous STM study[2] showed that in Bi_2Se_3 crystals grown at high temperatures (>800 C°), the most dominant defects were vacancies in the middle of a QL with the proposed explanation being that when the crystal is cooled, Se2 vacancies remain in Se2 positions due to a high energy barrier. Our calculations support this scenario and predict a high energy barrier of 1.99 eV for a vacancy to move from the middle of a QL (V^{Se2}) to the outer layer (V^{Se1}). In addition to the fact that vacancies do not agglomerate, the results imply that vacancies will tend to be scattered randomly throughout the crystal in both Se1 and Se2 positions.

Figure S3(b-d) presents three types of intralayer migration of interstitial S or Se atoms. The first type (S^{int}-S^{int}) describes the movement of a split-interstitial S or Se atom along the edge of a QL with the path highlighted by the black arrow (**Figure S3b**). The results show that there is a relatively small energy barrier of around 0.36 eV for S to move from one interstitial position to the next. When the impurity is a self-interstitial Se atom, the respective barrier is at 0.26 eV overall which is in broad agreement with a previous theoretical study[7] that found 0.41 eV. Moreover, **Figure S3c** shows what happens when an interstitial impurity reaches the vicinity of a Se1 vacancy on the outside of the QL. The energy barrier for intralayer S^{int}-S^{Se1} transformation is only 0.17 eV and describes the kinetics for the annihilation of a Se1 vacancy by a S^{int} or Se^{int} atom. Via this nearly barrier-less process, the crystal gains an overall energy of 1.90 eV per vacancy annihilation, as indicated in the energy curve for the final position (**Figure S3c**). On the other hand, the interstitial atom can move in the vicinity of a vacancy in the middle layer of the QL (V^{Se2}) as depicted in **Figure S3d**. The calculated energy curve has an energy barrier of 1.00 eV for S^{int}-V^{Se2} and the same process has a barrier of 1.36 eV when the interstitial atom is instead of Se^{int}. The smaller energy penalty for S can be attributed to the fact that it is slightly smaller than selenium, therefore it requires less space in order to penetrate through the intermediate Bi layer. As this type of vacancy annihilation leads to a crystal with perfect stoichiometry, the final position in **Figure S3d** is more stable than the initial configuration by around 2.19 eV (2.16 eV) for S (Se).

The above results imply that interstitial S atoms will tend to fill in Se1 and Se2 vacancies, while for the V^{Se2} vacancy annihilation in particular, S^{int}-V^{Se2} is slightly favored over Se^{int}-V^{Se2} as there is an energy difference of around 0.34 eV between their respective barriers.
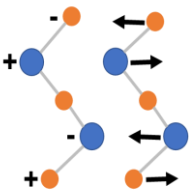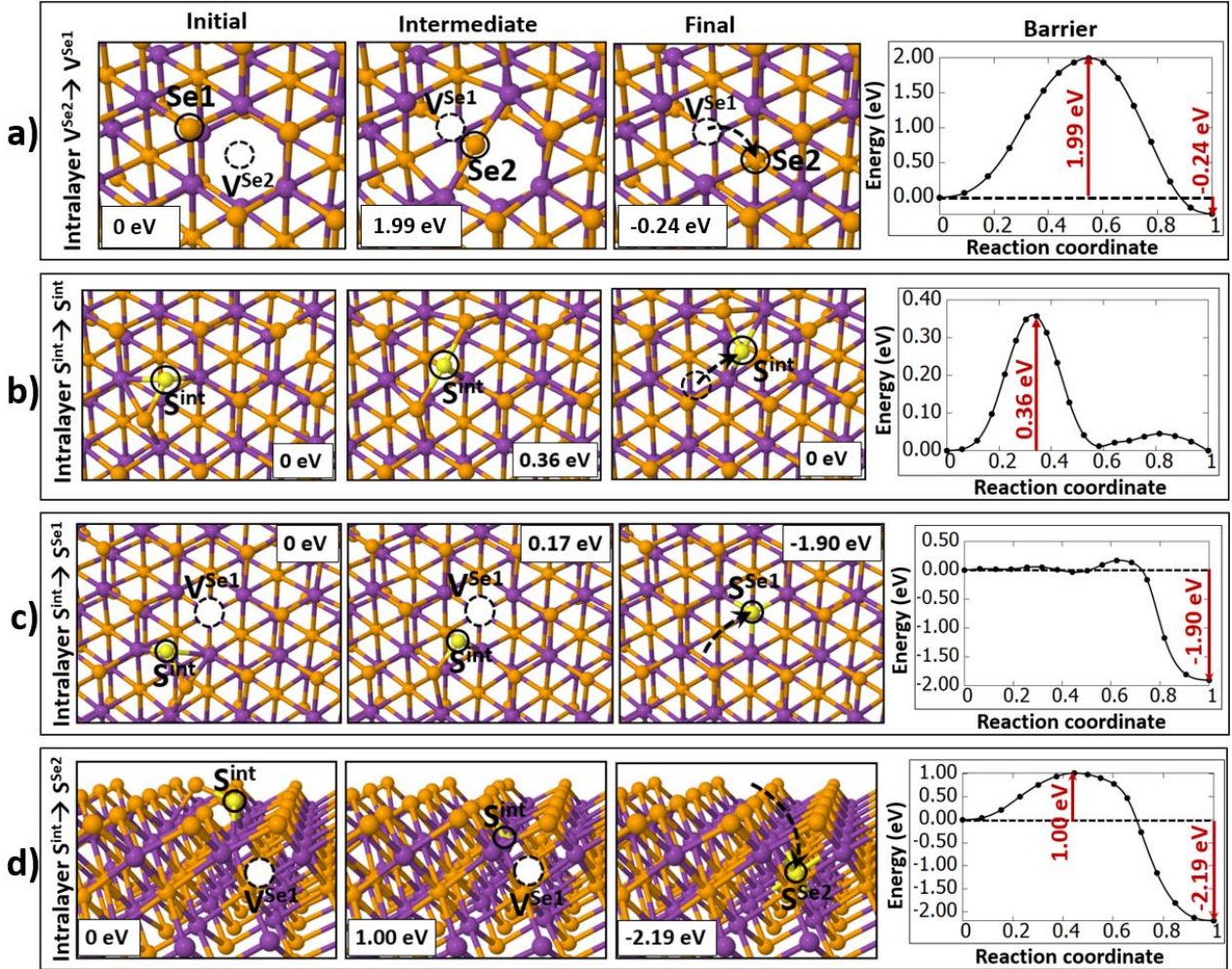
Figure S3. Simulated paths and their associated energy curves for intralayer diffusion of (a) Se vacancy or (b-d) an interstitial S atom. The initial and final configurations are shown along with an intermediate step which represents the position with the highest energy along the path. The black circles highlight the moving S, Se, or V^{Se} vacancy and the energies represent the relative stability with respect to the initial configuration (lower values are more stable).

4. Raman spectroscopy

Measurements of the Raman spectra of $Bi_2Se_{(3-x)}S_x$, Bi_2Se_3, and Bi_2S_3 were conducted at room temperature using LabRam HR Evolution from Horiba Scientific. The samples were excited by lasers with an excitation wavelength of 532 nm and 633 nm.

The detected Raman modes of monolayer and bulk sulfur alloyed Bi_2Se_3 compared to pure exfoliated Bi_2Se_3 are detailed in **Table S1**:

| Raman Mode	Raman shift [cm^{-1}]		
	Bi$_2$Se$_3$	Monolayer Bi$_2$Se$_{(3-x)}$S$_x$	Bulk Bi$_2$Se$_{(3-x)}$S$_x$
A_{1g}^1	71.37	68.92	72.18
E_g^2	130.3	127.9	132.5
A_{1g}^2	173.3	170.4	174.4

Table S1. Exfoliated and sulfur alloyed Bi$_2$Se$_3$ Raman modes.

5. X-ray diffraction (XRD)

Pure exfoliated and sulfur-alloyed Bi$_2$Se$_3$ samples were subjected to XRD measurements. The main peaks were identified and assigned to the corresponding crystallographic planes (**Figure S4a**).

To further verify the structure of the grown alloys, the XRD patterns were compared to those calculated for the ordered rhombohedral (**Figure S4c top panel**) and the most stable orthorhombic (**Figure S4c bottom panel**) structures of an alloy corresponding to x=1. The experimental results substantially match the calculated rhombohedral structure.
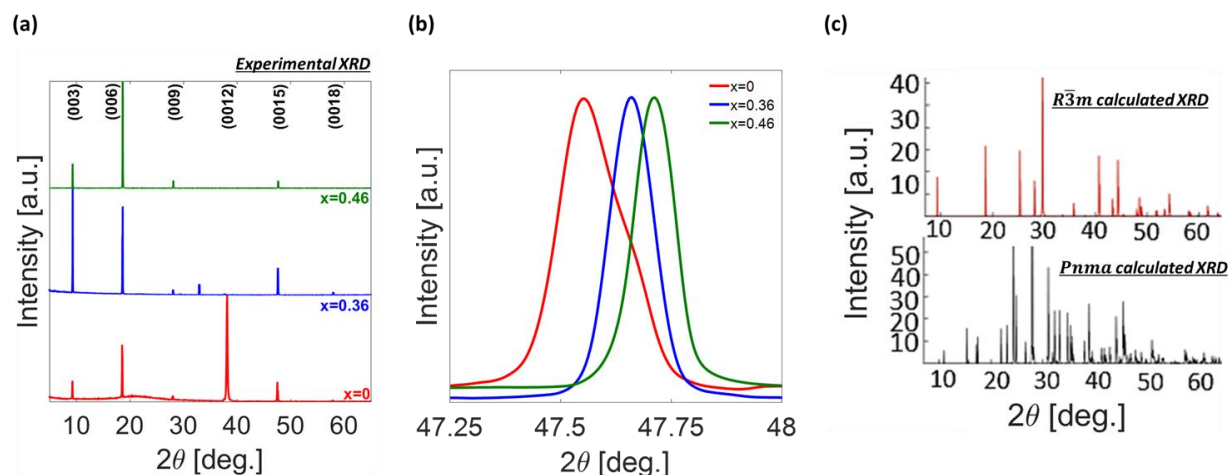
Figure S4. (a) Experimental XRD of $Bi_2Se_{(3-x)}S_x$ samples for varying values of x with the corresponding crystallographic planes. (b) Illustration of the shift in the crystallographic planes of the alloyed samples relative to those of Bi_2Se_3 (the crystallographic plane 0015 is given as an example). (c) Calculated XRD for the rhombohedral ($R\bar{3}m$) and the orthorhombic ($Pnma$) structures.

6. <u>Lattice parameters–sulfur content relation – Density Functional Theory (DFT) calculations</u>

To understand the trends in lattice parameters as a function of sulfur content, DFT calculations were performed using the Vienna Ab Initio Simulation Package (VASP).[8,9] The projector-augmented wave (PAW) method[10,11] was used to represent core and valence electrons with the valence electronic configurations for Bi, S, and Se being $5d^{10}6s^26p^3$, and $3s^23p^4$, $4s^24p^4$, respectively. Electron exchange and correlation were modeled using the PBEsol functional,[12] as this functional was found to produce relaxed lattice parameters ($a=b=4.13$ Å; $c=28.76$ Å) that are close to the experimental ones for the rhombohedral phase ($R\bar{3}m$) of Bi_2Se_3 ($a=4.14$-4.16 Å; $c=28.39$-28.77 Å).[13] To model varying S content, we used the virtual-crystal approximation (VCA)[14] wherein the PAW potentials of Se atoms are replaced by appropriately weighted linear combinations of Se and S potentials. The conjugate-gradient method was used to relax ionic positions and lattice vectors. Energy and force convergence criteria were set to 10^{-4} eV and 0.01 Å/eV, respectively. The kinetic energy cutoff was set to 400 eV and an 8×8×8 G-centered k-point mesh was used to sample the Brillouin zone in conjunction with a Gaussian smearing of 0.01 eV. **Figure S5** shows the c-axis spacing as a function of sulfur content, where the former was normalized by the experimental c-axis value of pure Bi_2Se_3 (**Table 2** of main text).
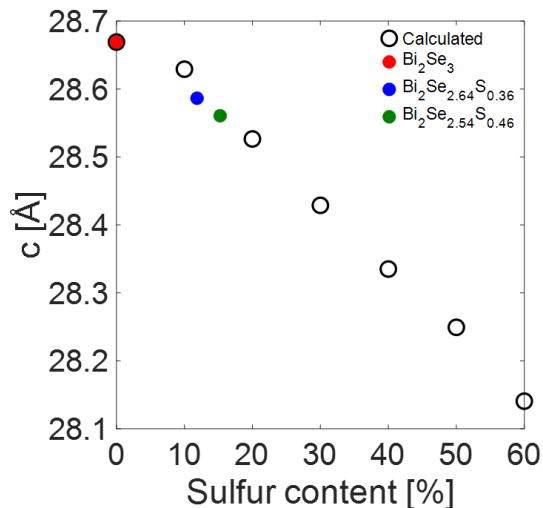
Figure S5. DFT calculated trend of the *c*-axis spacing as a function of sulfur content (hollow circles). Colored circles represent the experimental samples.

7. <u>Reflection measurements</u>

Reflection spectra of pure and sulfur alloyed Bi_2Se_3 samples were obtained using a Thermo Fisher Scientific Nicolet iS50R Fourier Transform Infrared (FTIR) spectrometer coupled to a Nicolet ContinuμM infrared microscope. Spectral range was set to 1,000-6,450 cm^{-1} using an Ever-Glo (20-9,600 cm^{-1}) source, an XT-KBr (375-11,000 cm^{-1}) beam splitter, and an MCT-A (600-11,700 cm^{-1}) detector. A 20× objective lens with NA=0.5 was used to focus light and collect spectra from the samples. Aperture size was set to fit the aperture of the samples. A high-quality gold mirror was used as a reference standard.

8. <u>Optical constants</u>

The optical constants of $Bi_2Se_{2.64}S_{0.36}$ thin film (thickness of ~360 nm) on a gold substrate were obtained by fitting the reflection spectrum 1,125-3,525 cm^{-1} with a 4-oscillator model (1 Drude and 3 Lorentz, **Figure S6**) using the RefFIT software.[15] Detailed fitting parameters are presented in **Table S2**.
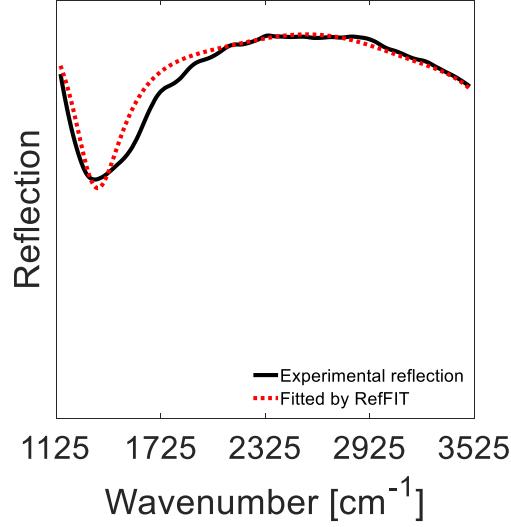
Figure S6. Reflection spectra (experimental and fitted) of exfoliated $Bi_2Se_{2.64}S_{0.36}$ on gold substrate.

Oscillator	ω_0 [eV]	ω_p [eV]	γ [eV]
Drude	-	0.001	0.003
Lorentz #1	0.733	0.007	0.115
Lorentz #2	0.276	0.054	0.144
Lorentz #3	0.389	0.079	0.131

Table S2. Oscillators parameters. ω_0, ω_p and γ are the transverse frequency, plasma frequency, and scattering rate, respectively. The high-frequency dielectric constant (ε_∞) was set to be 24.

9. <u>Temperature-dependent resistance measurements</u>

Temperature-dependent resistance measurements for $Bi_2Se_{(3-x)}S_x$ devices were performed in an RC102 Sample in Vacuum Continuous Flow Cryogenic Workstation Cryostat from Cryo Industries of America. The temperature of the system was controlled and monitored by a LakeShore 330 temperature controller via a 25-ohm heater and a DT-670 silicon diode thermometer which are closely connected to the sample holder with a cold finger made of oxygen-free high conductivity copper. With proper shielding from radiation and precise control of helium flow, the cryostat can reach a base temperature of 1.8K. An SR830 lock-in amplifier was used to measure the sample resistance. Simultaneously, the temperature was detected in the heat-up process from base temperature (3K) to 100K with a certain ramp rate.

REFERENCES

(1)   Henkelman, G.; Jónsson, H. Improved Tangent Estimate in the Nudged Elastic Band Method for Finding Minimum Energy Paths and Saddle Points. *Journal of Chemical Physics* **2000**, *113* (22), 9978–9985. https://doi.org/10.1063/1.1323224.

(2)   Dai, J.; West, D.; Wang, X.; Wang, Y.; Kwok, D.; Cheong, S. W.; Zhang, S. B.; Wu, W. Toward the Intrinsic Limit of the Topological Insulator Bi2Se3. *Phys Rev Lett* **2016**, *117* (10), 31–33. https://doi.org/10.1103/PhysRevLett.117.106401.

(3)   Wang, S.; Zhang, P. Native Point Defects in Bi2Se3: A First-Principles Study. *Physics Letters, Section A: General, Atomic and Solid State Physics* **2020**, *384* (14), 126281. https://doi.org/10.1016/j.physleta.2020.126281.

(4)   Xue, L.; Zhou, P.; Zhang, C. X.; He, C. Y.; Hao, G. L.; Sun, L. Z.; Zhong, J. X. First-Principles Study of Native Point Defects in Bi2Se 3. *AIP Adv* **2013**, *3* (5). https://doi.org/10.1063/1.4804439.

(5)   West, D.; Sun, Y. Y.; Wang, H.; Bang, J.; Zhang, S. B. Native Defects in Second-Generation Topological Insulators: Effect of Spin-Orbit Interaction on Bi 2Se 3. *Phys Rev B Condens Matter Mater Phys* **2012**, *86* (12), 1–4. https://doi.org/10.1103/PhysRevB.86.121201.

(6)   Scanlon, D. O.; King, P. D. C.; Singh, R. P.; De La Torre, A.; Walker, S. M. K.; Balakrishnan, G.; Baumberger, F.; Catlow, C. R. A. Controlling Bulk Conductivity in Topological Insulators: Key Role of Anti-Site Defects. *Advanced Materials* **2012**, *24* (16), 2154–2158. https://doi.org/10.1002/adma.201200187.

(7)   Kim, Y.; Lee, G.; Li, N.; Seo, J.; Kim, K. S.; Kim, N. Signature of Multilayer Growth of 2D Layered Bi2Se3 through Heteroatom-Assisted Step-Edge Barrier Reduction. *NPJ 2D Mater Appl* **2019**, *3* (1), 1–6. https://doi.org/10.1038/s41699-019-0134-2.

(8)   Kresse, G.; Furthmiiller B ', J. *Efficiency of Ab-Initio Total Energy Calculations for Metals and Semiconductors Using a Plane-Wave Basis Set*; 1996; Vol. 6.

(9)   Kresse, G.; Furthmü, J. *Efficient Iterative Schemes for Ab Initio Total-Energy Calculations Using a Plane-Wave Basis Set*; 1996.

(10)   Blochl, P. E. *Projector Augmented-+rave Method*; Vol. 50.

(11)   Kresse, G.; Joubert, D. *From Ultrasoft Pseudopotentials to the Projector Augmented-Wave Method*.

(12) Perdew, J. P.; Ruzsinszky, A.; Csonka, G. I.; Vydrov, O. A.; Scuseria, G. E.; Constantin, L. A.; Zhou, X.; Burke, K. Restoring the Density-Gradient Expansion for Exchange in Solids and Surfaces. *Phys Rev Lett* **2008**, *100* (13). https://doi.org/10.1103/PhysRevLett.100.136406.

(13) NAKAJIMA, S. The Crystal Structure of Bi2Te3-XSex. *J. Phys. Chem. Solids* **1963**, *24*, 479–485.

(14) Bellaiche, L.; Vanderbilt, D. *ARTICLES Virtual Crystal Approximation Revisited: Application to Dielectric and Piezoelectric Properties of Perovskites*.

(15) Kuzmenko, A. B. Kramers-Kronig Constrained Variational Analysis of Optical Spectra. *Review of Scientific Instruments* **2005**, *76* (8), 1–9. https://doi.org/10.1063/1.1979470.